J. Fluid Mech. (2011), *vol.* 672, *pp.* 130–146. © Cambridge University Press 2011
doi:10.1017/S0022112010005938

Radiative instability of the flow around a rotating cylinder in a stratified fluid

XAVIER RIEDINGER, STÉPHANE LE DIZÈS† AND PATRICE MEUNIER

Institut de Recherche sur les Phénomènes Hors Équilibre,
CNRS/Universités Aix-Marseille I and II,
49, rue F. Joliot-Curie, BP 146, F-13384 Marseille CEDEX 13, France

(Received 28 May 2010; revised 29 September 2010; accepted 10 November 2010;
first published online 7 February 2011)

The stability of the flow around a rotating cylinder in a fluid linearly stratified along the cylinder axis is studied numerically and experimentally for moderate Reynolds numbers. The flow is assumed potential and axisymmetric with an angular velocity profile $\Omega = 1/r^2$, where r is the radial coordinate. Neglecting density diffusion and non-Boussinesq effects, the properties of the linear normal modes are first provided. A comprehensive stability diagram is then obtained for Froude numbers between 0 and 3 and Reynolds numbers below 1000. The main result is that the potential flow, which is stable for a homogeneous fluid, becomes unstable for Froude number close to one and for Reynolds numbers larger than 360. The numerical results are then compared with experimental results obtained using shadowgraph and synthetic Schlieren techniques. Two symmetrical helical modes are found to be simultaneously unstable. We show that these modes exhibit an internal gravity wave structure extending far from the cylinder in agreement with the theory. Their wavelength and frequency are shown to be in good agreement with the numerical predictions for a large range of Froude and Reynolds numbers. These experimental results are the first indisputable evidence of the radiative instability.

Key words: stratified flows, vortex instability, waves in rotating fluids

1. Introduction

Stratified and rotating flows are widely studied, mostly for their geophysical relevance. The potential flow around a rotating cylinder, as it is the simplest of these flows, is fundamentally very interesting. Here, we numerically analyse its stability in the presence of viscosity and provide the first experimental evidence of its destabilisation.

The stability of rotating flows has been widely studied for Taylor–Couette systems. The effect of the stratification on the well-known Taylor–Couette instability leading to the appearance of axisymmetrical rolls was first shown to be stabilising (Ooyama 1966; Thorpe 1966; Withjack & Chen 1974, 1975; Boubnov, Gledzer & Hopfinger 1995; Caton, Janiaud & Hopfinger 2000; Billant & Gallaire 2005). Then, it was demonstrated that a stratified Taylor–Couette system could become unstable with respect to non-axisymmetric modes even when the Rayleigh criterion for centrifugal instability was not satisfied (Molemaker, McWilliams & Yavneh 2001; Yavneh, McWilliams & Molemaker 2001; Shalybkov & Rüdiger 2005; Le Bars & Le Gal 2007). This

---

† Email address for correspondence: ledizes@irphe.univ-mrs.fr

instability is now called the strato-rotational instability or SRI (Dubrulle *et al.* 2005). As shown by Yavneh *et al.* (2001) and Le Dizès & Riedinger (2010), the destabilisation results from a resonance between two waves localised near each cylinder. When the outer cylinder is removed, no resonance is possible any more but an inviscid instability is still present (Le Dizès & Riedinger 2010). This instability, which is associated with the spontaneous emission of internal gravity waves (Le Dizès & Billant 2009), is the subject of this paper. Although this instability could also be termed SRI, we think that it is more adequate to call it 'radiative instability' as for a vortex (Le Dizès & Billant 2009).

In the geophysical community, this instability has often been associated with negative energy waves (Schecter & Montgomery 2004; Schecter 2008) and over-reflection (Lindzen & Barker 1985). For stratified vortices, the instability mechanism has been recently rediscussed in the framework of a large wavenumber Wentzel–Kramers–Brillouin–Jeffreys (WKBJ) approach (Billant & Le Dizès 2009; Le Dizès & Billant 2009). In these articles, the dual role of the critical points has also been pointed out. The dependence of the instability with respect to the Froude and Reynolds numbers has been analysed by Riedinger, Le Dizès & Meunier (2010*a*) for a Lamb–Oseen vortex. Experimental results for this vortex have been obtained by Riedinger, Meunier & Le Dizès (2010*b*). Here, the stability properties of the potential flow will be compared with those of the Lamb–Oseen vortex and several differences will be pointed out. Le Dizès & Riedinger (2010) have analysed the stability of the rotating potential flow in an inviscid framework. In the present study, we address the stability of the flow for relatively low Reynolds numbers ($Re < 1000$) and provide the first experimental evidence of the instability.

The radiative instability is known in other physical contexts. It is present in compressible flows subject to acoustic radiation (Broadbent & Moore 1979; Luo & Sandham 1997; Parras & Le Dizès 2010) and in shallow-water flows radiating surface gravity waves (Satomura 1981; Hayashi & Young 1987; Ford 1994; Knessl & Keller 1995; Balmforth 1999). It has also been discussed in the context of superfluids (Roberts 2003) and astrophysical objects (Narayan, Goldreich & Goodman 1987).

The radiative instability is different from the centrifugal instability (Billant & Gallaire 2005), the elliptic instability (Guimbard *et al.* 2010), the zigzag instability (Billant & Chomaz 2000) and the tilt-induced instability (Boulanger, Meunier & Le Dizès 2008), which can all be present in a rotating stratified flow.

The paper is organised as follows. Section 2 provides the theoretical framework of the analysis. The base flow characteristics, the perturbation equations and the numerical technique are presented. Section 3 summarizes the numerical results. Growth rate, wavelength and frequency of the most unstable mode are obtained for a large range of Reynolds and Froude numbers. Its spatial structure is also provided. The differences with respect to the stability results of the Lamb–Oseen vortex are also emphasized in this section. In § 4, the main results of an experimental study are provided. The experimental set-up is first presented together with the visualisation techniques. Experimental estimates for the frequency and the wavelength of the observed unstable mode are then given and compared with the numerical predictions. A brief conclusion is finally made in the last section.

2. Framework

2.1. *Base flow, perturbation equations and numerical approach*

We consider the axisymmetric flow around a vertical cylinder of radius R_0 and infinite length, rotating at angular velocity Ω_0 in a viscous fluid of kinematic viscosity ν, stably stratified along the cylinder axis. The stratification is assumed to be linear with a constant Brunt–Väisälä frequency $N=\sqrt{-g\partial_z\rho/\rho_0}$. The base flow is potential and satisfies the Navier–Stokes equations under the Boussinesq approximation (Boulanger, Meunier & Le Dizès 2007). It is defined by two parameters, the Reynolds number Re and the Froude number F given, respectively, by

$$Re=\frac{\Omega_0R_0^2}{\nu}, \tag{2.1a}$$

$$F=\frac{\Omega_0}{N}. \tag{2.1b}$$

The diffusion of the density is neglected. Using R_0 and $1/\Omega_0$ as characteristic spatial and temporal scales, the angular velocity profile of the flow can be written as

$$\Omega(r)=\frac{1}{r^2}, \tag{2.2}$$

where r is the radial coordinate.

Infinitesimal disturbances of the velocity, pressure and density fields are considered in the form of normal modes

$$(u',v',w',p',\rho')=[u(r),v(r),w(r),p(r),\rho(r)]\exp(\mathrm{i}kz+\mathrm{i}m\theta-\mathrm{i}\omega t), \tag{2.3}$$

where u', v' and w' are the radial, azimuthal and axial velocities respectively, k and m are the axial and azimuthal wavenumbers, and ω is the complex frequency. The normal-mode amplitudes satisfy the following equations obtained by linearising the Navier–Stokes equations under the Boussinesq approximation around the base flow defined by (2.2):

$$\mathrm{i}\Phi u-2\Omega v=-\frac{\mathrm{d}p}{\mathrm{d}r}+\frac{1}{Re}\left(\Delta u-\frac{u}{r^2}-\frac{2\mathrm{i}m}{r^2}v\right), \tag{2.4a}$$

$$\mathrm{i}\Phi v=-\frac{\mathrm{i}mp}{r}+\frac{1}{Re}\left(\Delta v-\frac{v}{r^2}+\frac{2\mathrm{i}m}{r^2}u\right), \tag{2.4b}$$

$$\mathrm{i}\Phi w=-\mathrm{i}kp-\frac{1}{F^2}\rho+\frac{1}{Re}\Delta w, \tag{2.4c}$$

$$\mathrm{i}\Phi\rho=w, \tag{2.4d}$$

$$\frac{1}{r}\frac{\mathrm{d}(ru)}{\mathrm{d}r}+\frac{\mathrm{i}mv}{r}+\mathrm{i}kw=0, \tag{2.4e}$$

where

$$\Delta=\frac{\partial^2}{\partial r^2}+\frac{1}{r}\frac{\partial}{\partial r}-k^2-\frac{m^2}{r^2} \tag{2.5}$$

is the Laplacian operator written in cylindrical coordinates and

$$\Phi=-\omega+m\Omega. \tag{2.6}$$

This system can be further reduced by eliminating pressure and axial velocity to obtain a third-order system of the form $\omega A\boldsymbol{f}=B\boldsymbol{f}$, for $\boldsymbol{f}=[u(r),v(r),\rho(r)]$. The fields u, v and ρ must also satisfy boundary conditions: on the cylinder

$$u(r=1)=v(r=1)=\frac{\mathrm{d}u}{\mathrm{d}r}(r=1)=0, \tag{2.7}$$

and at infinity, u, v and ρ must either vanish or be an outward wave. The reduced system, together with the above boundary conditions, defines a generalized eigenvalue problem for the frequency ω, for fixed base flow parameters (Re, F) and fixed real axial wavenumber k and azimuthal wavenumber m.

The two symmetries of the equations $(m, \omega, k, u, v, w, \rho, p) \rightarrow (m, \omega, -k, u, v, -w, -\rho, p)$ and $(m, \omega, k, u, v, w, \rho, p) \rightarrow (-m, -\bar{\omega}, k, \bar{u}, \bar{v}, -\bar{w}, -\bar{\rho}, \bar{p})$ allow us to limit the study to positive values of the axial wavenumber, k, and the azimuthal wavenumber, m. The objective is to determine the unstable eigenmodes, that is, those with a positive growth rate $\omega_i = \mathrm{Im}\, m(\omega)$, when the four parameters Re, F, k and m are varied. Because we want to provide the marginal curves of the unstable modes, neutral and weakly damped eigenfrequencies are also considered.

The numerical code is a Chebychev spectral collocation code. It is similar to the code used by Fabre, Sipp & Jacquin (2006) for a homogeneous vortex and adapted by Riedinger *et al.* (2010*a*) for a stratified vortex. As explained by Riedinger *et al.* (2010*a*), the condition of radiation is applied to the modes by considering a complex integration path. This allows us to obtain eigenvalues for modes which are not necessarily bounded in the physical space and thus to consider neutral and weakly damped modes. For the present flow, we have used the following mapping between the Chebychev variable ξ and the complex radial coordinate:

$$r = 1 + L\frac{1+\xi}{1-\xi}\,\mathrm{e}^{\mathrm{i}\pi/10}, \tag{2.8}$$

where L is a parameter modifying the coordinate of the last collocation point before infinity. Typically, we have used $N_p = 120$ collocation points and $L = 3.43$, such that $r_{max} \simeq 20\,000\,\mathrm{e}^{\mathrm{i}\pi/10}$.

3. Numerical results

The inviscid stability properties of the stratified potential flow have been considered in Le Dizès & Riedinger (2010). It was shown that for $Re = \infty$ there exists an infinity of unstable modes for any non-zero azimuthal wavenumber m. The most unstable inviscid modes have been found to be obtained for large values of m and to be localised near the rotating cylinder. Moreover, it was also shown that the inviscid instability is maximal in the limit of small F. In this limit, the maximum growth rate converges to a constant value and the wavenumber of the fastest-growing mode scales as m/F. The instability does not disappear for large F but both the wavelength and the growth rate of the unstable modes scale as $1/F$ for large F.

When viscosity is introduced, high wavenumbers are stabilized, which damps the instability at low Froude number. This substantially modifies the characteristics of the instability for moderate Froude numbers. For example, for $F = 0.5$, the critical Reynolds number below which the modes $m = 10$, 5, 2 and 1 are stabilized are $Re = 47\,000$, $11\,000$, 2200 and 1015, respectively. For the Reynolds numbers of the experiment described below, only helical modes $m = 1$ are unstable. In figure 1, we have plotted the characteristics of the first helical modes for a fixed Froude number $F = 1.25$, and two Reynolds numbers. The frequency of these modes satisfies $\max(0, 1 - 1/F) < \omega_r < 1$. For $Re = \infty$, only the first three branches have been plotted. Note that all these inviscid modes are unstable in an infinite band of wavenumbers. As explained by Le Dizès & Riedinger (2010), these modes are discretized by the number of oscillations of their radial structure in the region localised between the cylinder and the turning point $r_c = \sqrt{m/\omega}$, where the local inertial frequency $\omega - m\Omega(r)$ of the mode vanishes. These modes also possess a radiative structure far from the cylinder, which is responsible for their unstable character (Le Dizès & Billant 2009; Le Dizès

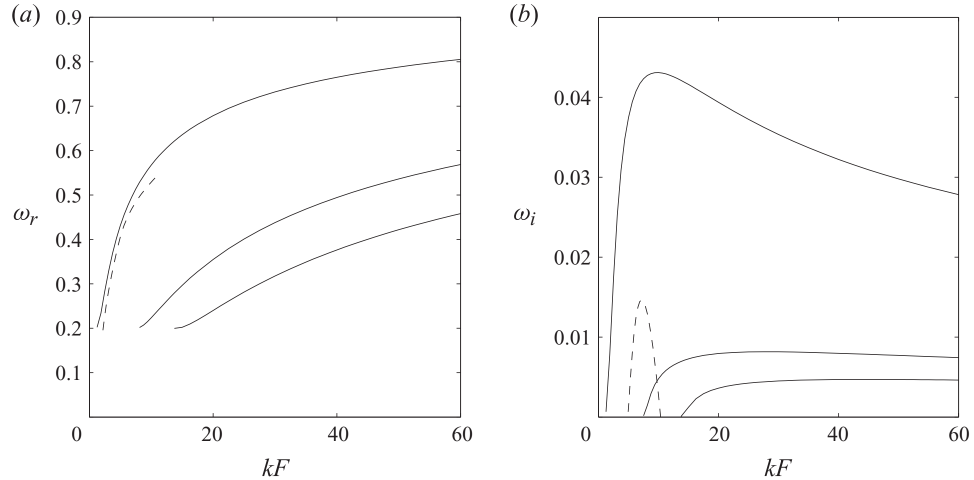

FIGURE 1. Dispersion relations of the helical modes ($m = 1$) of the rotating potential flow for $F = 1.25$, for $Re = \infty$ (solid line, first three modes only) and for $Re = 1000$ (dashed line). (a) Frequency $\omega_r = \mathrm{Re}\, e(\omega)$ versus kF, (b) growth rate $\omega_i = \mathrm{Im}\, m(\omega)$ versus kF.

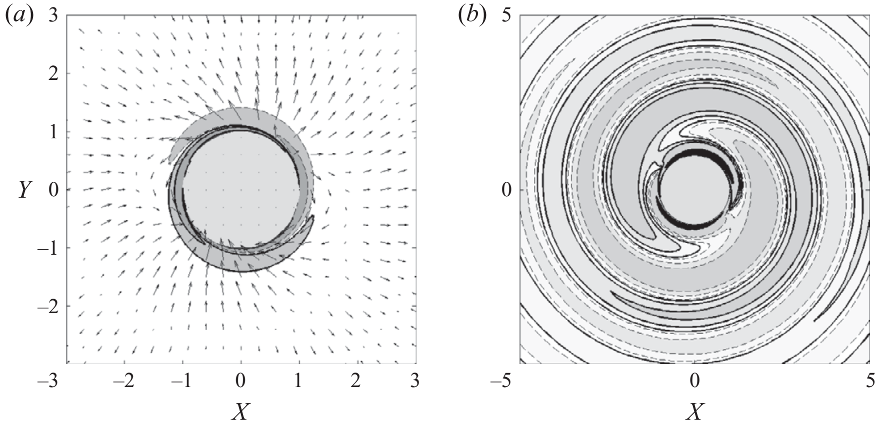

FIGURE 2. Structure of the most unstable mode (corresponding to $k \approx 5.8$, $\omega \approx 0.478 + \mathrm{i}0.0147$) for $Re = 1000$ and $F = 1.25$. (a) Vorticity contours and velocity vector field (indicated by arrows), (b) density contours.

& Riedinger 2010). Both the radiative structure and the mode discretization are not affected by viscosity. This can be seen in figure 2, which shows the vorticity and density fields of the most unstable mode obtained for $Re = 1000$ and $F = 1.25$. Both the localisation near the cylinder and the fact that there is a single half oscillation between the cylinder and the turning point $r_c \approx 1.45$ (as expected for the first mode) are visible on the vorticity plot (figure 2a). The radiative zone extending far from the cylinder is by contrast visible on the density plot (figure 2b). It leads to a density pattern, in a longitudinal plane containing the cylinder axis, of the form illustrated in figure 3.

Viscosity mainly affects the growth rate of the modes. As seen in figure 1, only the first branch remains unstable in a small wavenumber interval for $Re = 1000$. The maximum growth rate has decreased by a factor 3 compared with the inviscid case, but the frequency has varied very little. For each value of Re and F, a maximal

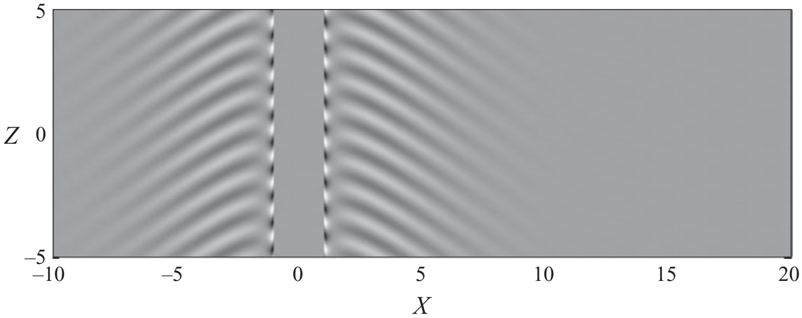

FIGURE 3. Vertical density gradient pattern associated with the most unstable mode for $Re = 1000$ and $F = 1.25$. Only the mode propagating upwards has been represented. A symmetrical mode propagating downwards with the same growth rate exists.

growth rate with respect to k can be obtained. The maximal growth rate contours when both F and Re are varied are displayed in figure 4(*a*). The region of stability corresponds to the white region of this figure, where the maximum growth rate is negative. At a given Reynolds number, the potential flow is unstable in a band of Froude numbers around 1. The unstable band of Froude numbers diminishes when the Reynolds number decreases and ultimately disappears at a critical Reynolds number $Re_c \approx 360$, below which the potential flow is stable whatever the Froude number. The axial wavenumber and frequency corresponding to the maximum growth rate are shown in figures 4(*b*) and 4(*c*), respectively. The frequency is fairly constant and only increases from 0.28 to 0.5 when the Froude and Reynolds numbers increase on the range studied here. The axial wavenumber increases by a factor 2 when the Froude number decreases (as can be deduced from inviscid results) and the Reynolds number increases.

As shown by Le Dizès & Billant (2009) and Riedinger *et al.* (2010*a*), the instability of the flow around a rotating cylinder is also present in vortices such as the Lamb–Oseen vortex. There are however some differences which are worth pointing out. First, note that the Lamb–Oseen vortex as well as any other free vortex possesses an unstable mode which is not present in the rotating potential flow. This mode is a helical mode which is unstable for a small wavenumber only (even in the inviscid limit). It has been termed ‘displacement mode’ as it corresponds to a global displacement of the vortex in the limit $k = 0$. This mode is not present in the case of the potential flow because the rotating cylinder generating the potential flow cannot be moved. For the Lamb–Oseen vortex, this mode is almost always the most unstable mode (Riedinger *et al.* 2010*a*). The exception is for large Froude and Reynolds numbers. In contrast with the unstable modes of the flow around the rotating cylinder, this displacement mode can be unstable whatever the Reynolds number, which means that the Lamb–Oseen vortex has no critical Reynolds number.

Second, the Lamb–Oseen vortex possesses other unstable modes which resemble the unstable modes of the rotating potential flow. These modes have been termed ‘ring modes’ (Le Dizès & Billant 2009). As shown by Le Dizès & Billant (2009), they are well-described by a WKBJ analysis in the limit of large axial wavenumbers in which they are discretized by the number of oscillations of their radial structure between two turning points. As for the helical modes of the rotating potential flow, they also possess a radiative structure which is responsible for their unstable character. Although they are qualitatively similar, the modes of the potential flow are much

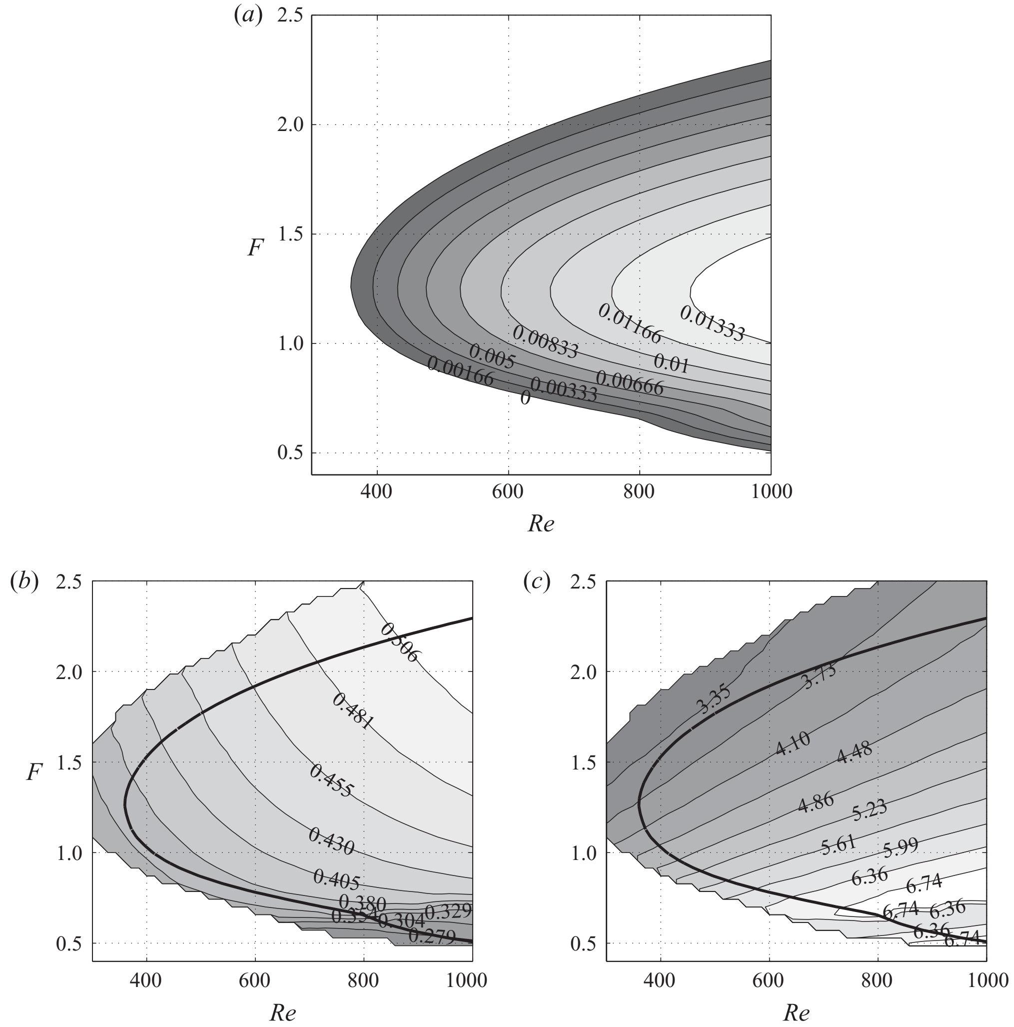

FIGURE 4. Characteristics of the most unstable mode (first helical mode) for fixed Re and F. (a) Isocontours of the growth rate ω_i. (b) Isocontours of the frequency ω_r. (c) Isocontours of the axial wavenumber k. In (b) and (c) the black line indicates the limit of the stability domain.

more unstable. Their maximum inviscid growth rate is 20 times larger and is reached for a smaller wavenumber. Their frequency is also larger.

4. Experimental results

4.1. *Experimental set-up and visualisations*

The experiment is performed in a tank of dimension $L \times l \times h = 240 \times 74 \times 48\,\mathrm{cm}^3$. The fluid is linearly stratified with salted water on a depth of 45 cm. The stratified medium is obtained using the classical filling method using two tanks, one with pure water and the other with salted water. The same filled tank was used for several experiments during one month. During this period, we checked that the stratification in the middle part of the tank (between 10 and 30 cm) did not change and remained uniform with a constant Brunt–Väisälä frequency $N \approx 1.63 \pm 0.03\,\mathrm{rad\,s^{-1}}$. However,

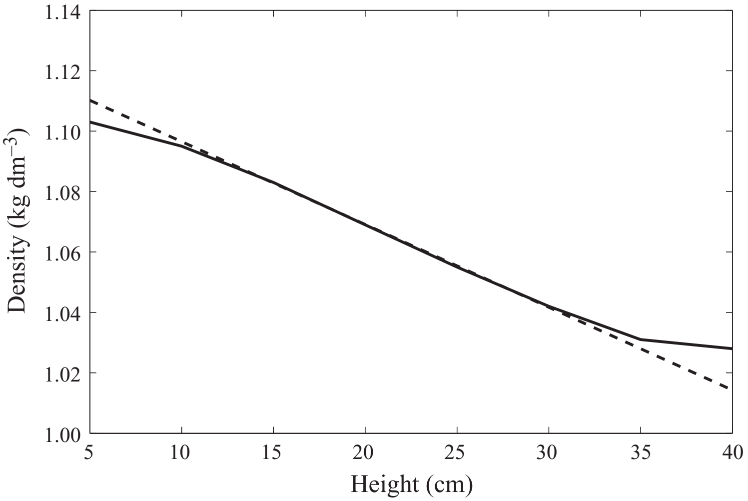

FIGURE 5. Density (kg dm^{-3}) as a function of height (cm) for the first experiment (dashed line) and after one month of experiments (solid line). Here, the mean Brunt–Väisälä frequency is $N = 1.6\,\mathrm{rad\,s^{-1}}$.

we did observe that the stratification at the top (35–45 cm) and the bottom (0–10 cm) does vary because of salt diffusivity, turbulent mixing and evaporation. This effect can be seen in figure 5, where the density is plotted versus the depth for the first experiment and after one month of experiments. Mixing and diffusion tend to decrease the Brunt–Väisälä frequency near the top and bottom of the tank. This effect will explain some of the observations presented below. During the month of experiments, we also regularly checked the temperature of the fluid.

The flow is created by rotating a vertical stainless steel cylinder in the tank. Three cylinders of radius $R_0 = 20, 15, 12.5$ mm have been used. For each experiment, the cylinder was progressively accelerated during 30 000 rad (i.e. 4774 rounds) with an angular velocity law given by

$$\dot{\theta} = \Omega_0 \left(\frac{\theta}{30\,000} \right)^{1/5}, \tag{4.1}$$

then kept at constant angular velocity Ω_0. Video recording and measurements were made after having reached a permanent regime, which was usually obtained after a rotation of 50 000 rad. During the transient stage, which could last several hours, strong $m = 0$ and $m = 1$ centrifugal modes were observed. These transitory instabilities induce a convective transfer of momentum which speeds up the formation of the potential flow.

The velocity field obtained after the transient phase has been measured by particle image velocimetry (PIV) in a horizontal plane in the middle of the tank to check the quality of the base flow. This was achieved by injecting small particles in the fluid, and illuminating them from the side with a pulsed YaG laser. Images were recorded and treated with the cross-correlation algorithm developed at IRPHE (Meunier & Leweke 2003). A typical illustration of the velocity vector field obtained by PIV is shown in figure 6(a). A few wrong vectors are visible around the cylinder and on the right of the cylinder between the two dashed lines, due to the shade of the cylinder in the laser sheet. By averaging on circles (excluding the region between the two

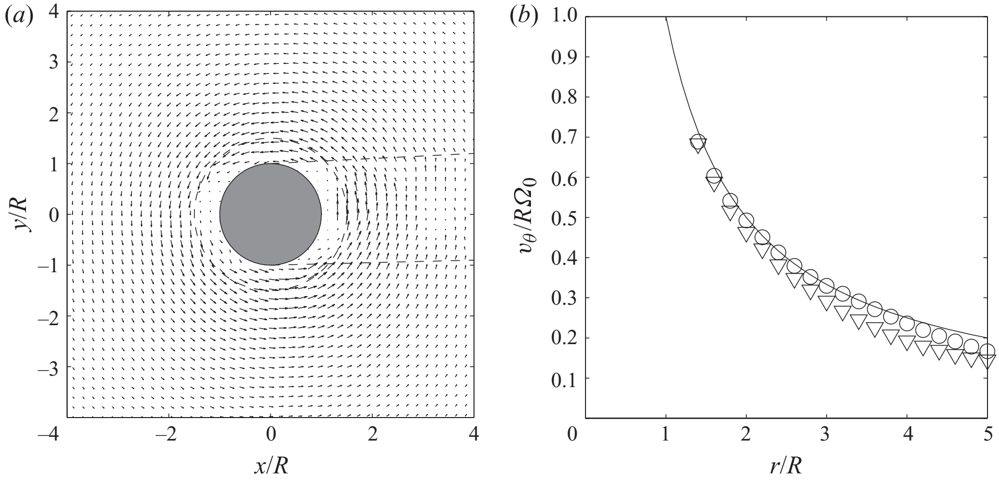

FIGURE 6. Base flow measurement by PIV. (*a*) Velocity vector field in a plane perpendicular to the cylinder axis. (*b*) Mean azimuthal velocity profile for a stable configuration (triangles, $Re = 279$, $F = 0.59$) and an unstable configuration (circles, $Re = 405$, $F = 0.88$). The potential flow profile $v_\theta = 1/r$ is plotted by the solid line.

dotted lines), we obtain a mean angular velocity field, which can be compared with (2.2). In figure 6(*b*), the mean azimuthal velocity profiles obtained for both a stable and unstable case have been plotted. We can see that in both cases the azimuthal velocity field is well approximated by the potential flow profile, although the velocity is slightly smaller, which is a remnant of the transient stage. Note however that the unstable configuration is slightly closer to the potential flow than the stable one.

Three different visualisation techniques have been used to observe and analyse the instability.

(i) Shadowgraph with a screen of tracing paper on the back of the tank for a large field of view.

(ii) Shadowgraph without tracing paper but through a 30 cm large lens for contrasted images on a smaller field of view.

(iii) Synthetic Schlieren for enhanced contrast far from the cylinder.

A comparison between the two shadowgraph techniques is provided in figure 7. While the shadowgraph with a screen of tracing paper shows the whole tank, it has a much lower sensitivity than the shadowgraph with the lens. Therefore, the shadowgraph with the tracing paper can be used to observe the development of the instability and boundary effects. On the other hand, using the lens results in images with a much higher contrast but only in a smaller section of the tank. The case shown in figure 7 corresponds to an unstable configuration. An internal gravity wave with an upward arrow shape rising and winding around the cylinder is visible. A thin structure attached to the cylinder which rises with the internal wave is also seen. These structures are antisymmetric with respect to the cylinder axis. The whole structure forms a helical structure with an $m = 1$ azimuthal symmetry. This is in agreement with the numerical results, which predict a most unstable mode with the same azimuthal wavenumber for these parameters.

Structures can be seen close to the cylinder along its entire height. Note, however, that the top and bottom regions are much more perturbed. This is probably not only due to the change of stratification in these layers (as mentioned above), but also

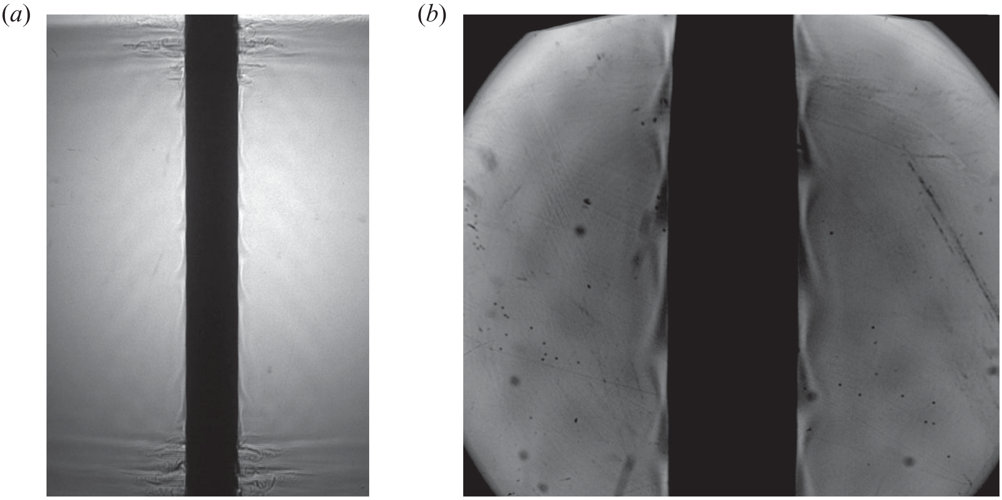

Figure 7. Typical shadowgraph visualisations (a) through a sheet of tracing paper and (b) through a lens. Here $Re = 715$ and $F = 2.05$.

due to the presence of the support of the cylinder which tends to produce horizontal vorticity. When the flow is stable, no density fluctuations are visible around the central part of the cylinder.

The shadowgraph with a lens is a more sensitive technique and has been used to measure the threshold of the instability with a good precision (figure 7b). Most of the measurements of wavelength and period of internal waves were done using this technique. In most cases, as in figure 7(b), two series of waves are seen with this visualisation technique, one oriented downwards and the other upwards. This is in agreement with the symmetry $k \rightarrow -k$ mentioned above, which guarantees that both upward and downward waves are simultaneously unstable with the same growth rate. This makes the undulating structures close to the cylinder pulsating rather than rising upwards. Nevertheless, in a few cases, we observed that one of the two waves can be dominant.

Quantitative data can be obtained from these visualisations by making a spatio-temporal diagram obtained by extracting a vertical line from each video frame located close to the cylinder over a duration of 180 s and showing the sequence of these lines. Figure 8 presents the spatio-temporal diagram corresponding to the experiment shown in figure 7. The pulsating structures, characteristic of standing waves, are clearly visible as alternating bright and dark patches at the same location (i.e. on a vertical line). They reveal the presence of two upward and downward waves which propagate along inclined paths parallel to the two grey lines. The period of the waves can be read on the vertical, their wavelengths on the horizontal. The angle of the grey lines gives the axial phase velocity of the waves V_ϕ. In practice, we measured the frequencies and the phase velocities, and we deduced the wavenumbers from $k = \omega / V_\phi$. We can see that there is a difference between the frequencies of the two opposite waves since similar patches are not aligned on vertical lines but slowly drift towards the top. The smooth angle ($\simeq 25^\circ$ in this figure) indicates the difference of frequency.

The third visualisation technique, the synthetic Schlieren, has been used to obtain visualisations as the one shown in figure 9(a). This technique is less precise than

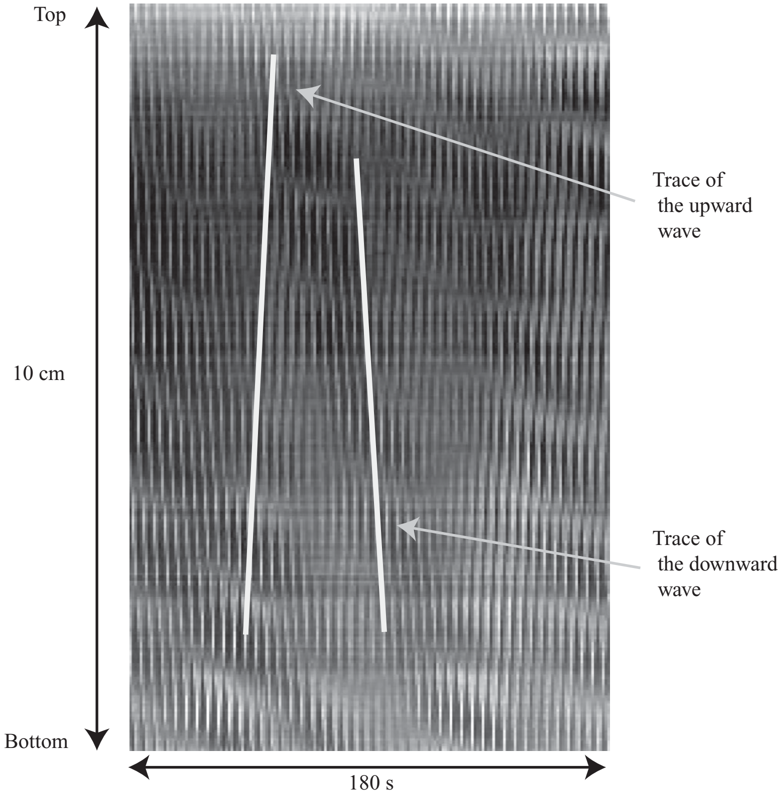

FIGURE 8. Typical spatio-temporal diagram obtained from the shadowgraph. Here for $Re = 715$ and $F = 2.05$.

the shadowgraph for wavelength measurements but it provides clearer pictures of the internal wave pattern in the far field. Synthetic Schlieren can provide either the vertical or the horizontal density gradient averaged along the depth of the tank. As we are looking at the perturbations of a cylindrical flow integrated along its depth, we *a priori* get a qualitative and not quantitative information on these perturbations. Nevertheless, we have been able to check that the theoretical relation $\cos \Phi = \omega / N$ between the wave frequency and the wave pattern angle in the far field was satisfied. Figure 9(a) shows an array of dark and bright patches, which once again reveal the presence of the upward and downward waves simultaneously excited. Note however that the downward wave is predominant at the top and the upward wave is predominant at the bottom.

Figure 9(b) is the pattern obtained by the superposition with the same amplitude of the two upward and downward most unstable linear modes computed for the experimental parameters. The dimensions of the pictures are identical: $40 \times 27\,\mathrm{cm}^2$. The similarity between the two figures is striking. A supplementary movie from which figure 9(a) is taken is available at journals.cambridge.org/flm.

The very good agreement between the numerical results and the experiments has been confirmed by other experiments. In particular, we have observed that the wave pattern becomes more vertical for larger Froude numbers, as expected from the theory.

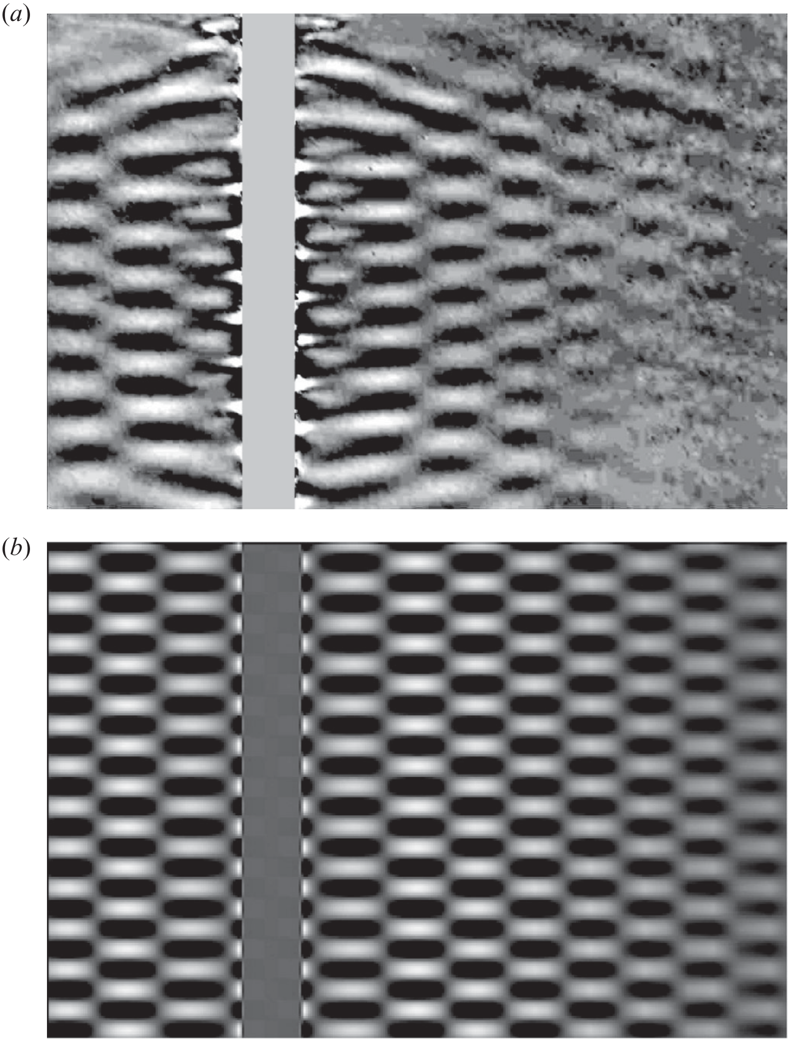

FIGURE 9. Vertical density gradient pattern associated with the instability for $Re = 343$ and $F = 1.01$. The grey vertical rectangle corresponds to the cylinder (of radius $R_0 = 15\,\mathrm{mm}$). (*a*) Experimental results obtained with synthetic Schlieren. (*b*) Numerical results obtained by the superimposition of both upward and downward most unstable waves with the same amplitude.

4.2. *Stability domains*

In figure 10, we present the comparison between the instability domain found numerically and the results of the different experiments. Circles correspond to unstable experiments and crosses to stable ones. We can see that the experimental instability domain exhibits the same shape as the numerical instability domain although it is slightly larger. The smallest unstable experimental Reynolds number $Re_{min} \simeq 240$ is obtained for Froude numbers around 1.25. No instability was observed for small Froude numbers ($Re = 325$, $F = 0.90$ and $Re = 396$, $F = 0.63$) and for large Froude numbers ($Re = 590$, $F = 2.5$ and $Re = 506$, $F = 2.12$). This clearly demonstrates that the instability is triggered by the stratification and is thus different from the centrifugal instability. In this figure, the values of the Reynolds and Froude numbers for each

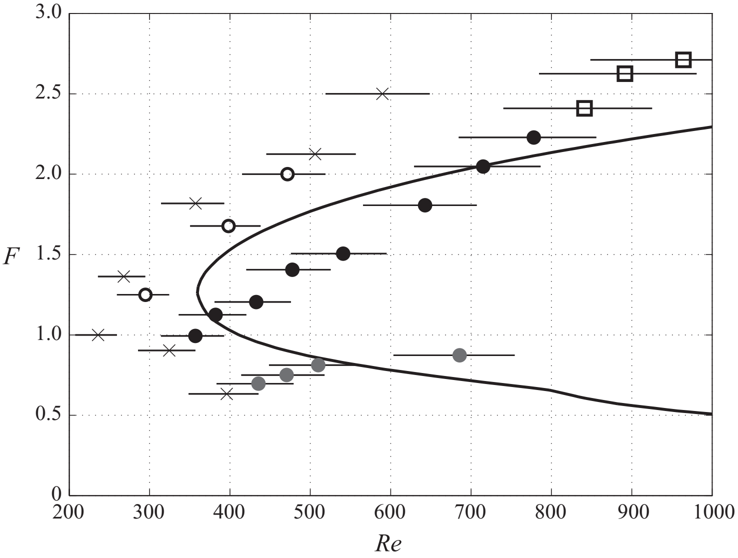

FIGURE 10. Comparison between numerical and experimental stability results. Symbols and lines: solid line, numerical prediction for the limit of the domain of instability; circles, unstable experiments where an internal wave pattern is visible; squares, unstable experiments but without a well-defined wave pattern; crosses, stable experiments; horizontal lines, the variations of the Reynolds number between the top and bottom of the tank due to its dependence with respect to the mean density. The three colours correspond to experiments with three different cylinder radii (grey, $R_0 = 20\,\mathrm{mm}$; black, $R_0 = 15\,\mathrm{mm}$; white, $R_0 = 12.5\,\mathrm{mm}$). The colour code is also used to differentiate the data which are reported in figure 11.

experiment are obtained using the characteristics of the flow at middle height of the cylinder. At the top of the tank the Reynolds number is larger and at the bottom it is smaller. This variation comes from the dependence of viscosity with salinity. This variation of the Reynolds number is indicated in figure 10 by the horizontal error bars. We can see that if we consider the extreme parts of the parameters, the experimental threshold is close to the numerical curve. The critical Reynolds number obtained numerically is $Re_c \approx 360$ and the experimental one is between 295 and 325.

We have also seen that the Brunt–Väisälä frequency is smaller at the top and bottom of the tank, which means that the Froude number is larger in these regions. This effect together with the boundary effect itself could explain the differences between the experimental and numerical stability domains. In particular, we have observed that the boundary effects become more and more important as the Reynolds number increases. The unstable configurations which are indicated by square symbols in figure 10 are dominated by boundary effects: thick turbulent regions near the top and bottom of the cylinder are observed instead of the typical internal wave structure observed in the other configurations.

It is also important to mention that the theory does consider neither nonlinearity nor transient, which are both present in the experiments. Nonlinear effects could be destabilizing. This means that if the instability bifurcation was subcritical, we would expect a smaller instability threshold than that predicted by the linear theory. Note also that in the experiment, we cannot control the time at which the instability develops. If the instability starts while the potential base flow is not fully established,

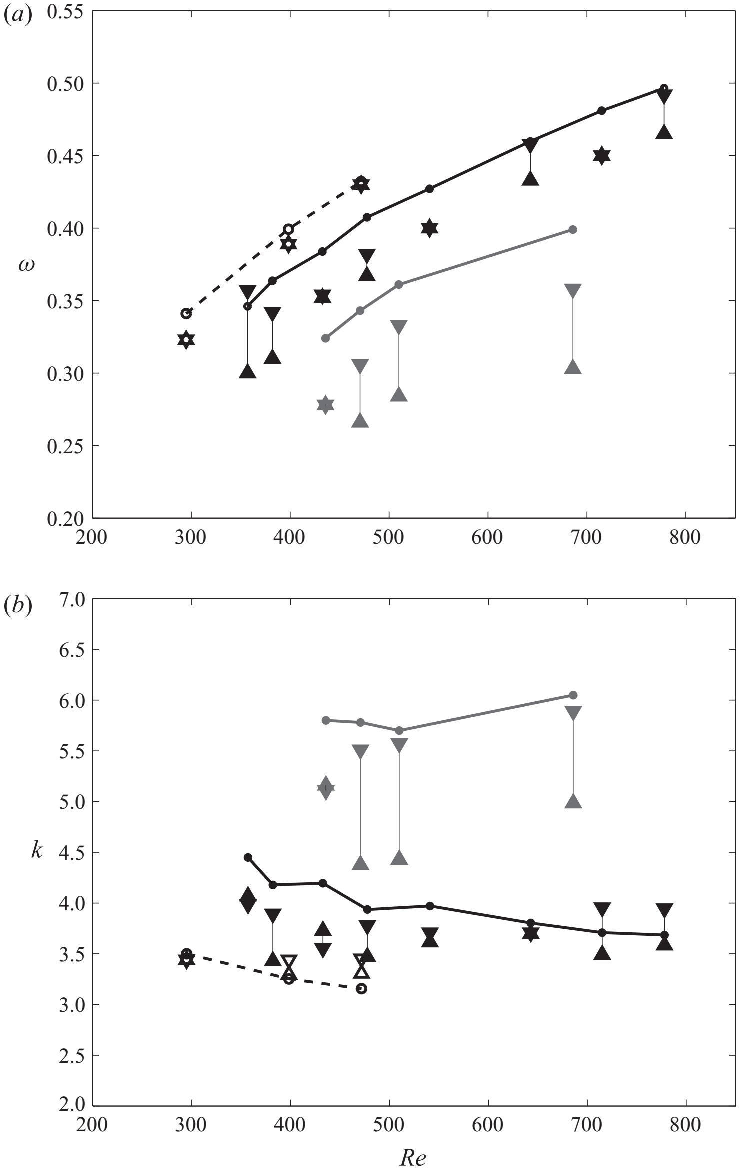

FIGURE 11. Comparison between numerical (lines with circles) and experimental (triangles) results for the unstable configurations shown in figure 10. (*a*) Frequency; (*b*) wavenumber. Upward triangle, experimental measurement for the upward wave; downward triangle, experimental measurement for the downward wave. The grey triangles correspond to $R_0 = 20$ mm and should be compared with the grey line. The black triangles correspond to $R_0 = 15$ mm and should be compared with the black line. The white (open) triangles correspond to $R_0 = 12.5$ mm and should be compared with the dashed line.

it is not impossible that it is boosted by the weak negative background vorticity which is still present.

4.3. *Comparison frequencies and wavelengths of the modes*

Wavelength and frequency measurements for the unstable configurations of figure 10 have been reported in figure 11.

They are represented with an upward (respectively downward) triangle for the upward (respectively downward) wave. They are compared with the numerical predictions obtained for the most unstable mode (or for the least stable mode) for the parameters of the experiment. The data have been plotted as a function of the Reynolds number with the colour code used in figure 10. For each set of experiments (given colour), the frequency of the instability mode is found to increase with the Reynolds number while its wavenumber is approximately constant. These trends are in agreement with the numerical results. Numerical predictions and experimental measurements are also found to be in good agreement quantitatively. We have obtained that the mean relative difference is 9.6 % for the frequencies and 9.5 % for the wavelengths. Yet, a better agreement has been systematically obtained for the wave propagating downwards. The frequency and the wavenumber of the upward wave were generally found to be smaller than those of the downward wave and the numerical prediction.

Some of these observations can be partly explained. First, we have already mentioned that the Reynolds number was slightly higher at the top of the tank than at its bottom. From figure 4(b,c), we also know that both the frequency and the wavenumber of the most unstable mode increase with the Reynolds number. We therefore expect the downward wave which is mainly excited close to the top to have larger frequency and wavelength than the upward wave which is mainly excited from the bottom. Moreover, we suspect, especially for the small Froude number cases (grey symbols), that the upward wave is forced by the cylinder support which is placed at the bottom of cylinder. This could explain why this wave is observed while the flow is in weakly stable configuration.

Finally, some of the discrepancies could also be associated with nonlinear effects which are systematically present in the experiments but not taken into account in the numerical computations.

5. Conclusion

The stability of the stationary flow generated by a rotating cylinder in a viscous stratified fluid has been examined. Assuming a potential flow profile $\Omega = 1/r^2$ for the angular velocity, we have first shown that the flow is *a priori* unstable with respect to the radiative instability for moderate Reynolds numbers. The complete numerical stability diagram has been obtained for Reynolds numbers $Re < 1000$ and Froude numbers $F < 3$. The most unstable mode has been shown to be a 3D helical mode ($m = 1$) with a radiative structure and its wavenumber and frequency have been computed. Experimental results have also been reported and the instability predicted by the theory has been observed. Frequency and wavenumber measurements of the instability mode have been made using shadowgraph and synthetic Schlieren techniques, and compared with the numerical predictions. A good agreement has been demonstrated.

The radiative instability had been previously observed in a free Lamb–Oseen-like vortex (Riedinger *et al.* 2010b). However, for such a vortex, the most unstable was a ‘displacement mode’ (see Riedinger *et al.* 2010a), which is not present in our configuration. In that experiment, owing to the viscous diffusion of the vortex, it had not been possible to provide good quantitative comparisons with numerical stability results. Moreover, the displacement mode is also the main ingredient of the zigzag instability (Billant & Chomaz 2000), which is active when a vortex interacts with neighbouring vortices. For this reason, it was difficult to be sure that the instability mode observed in Riedinger *et al.* (2010*b*) was not boosted by an interaction with the weak vorticity background which was minimized but not completely suppressed.

In the present experimental study, these two difficulties are absent as the base flow is stationary and does not possess the displacement mode. We are therefore very confident of our experimental results. We think that they constitute the first indisputable evidence of the radiative instability.

Supplementary movie is available at journals.cambridge.org/flm.

REFERENCES

Balmforth, N. J. 1999 Shear instability in shallow water. *J. Fluid Mech.* **387**, 97–127.

Billant, P. & Chomaz, J.-M. 2000 Experimental evidence for a new instability of a vertical columnar vortex pair in a strongly stratified fluid. *J. Fluid Mech.* **418**, 167–188.

Billant, P. & Gallaire, F. 2005 Generalized Rayleigh criterion for non-axisymmetric centrifugal instabilities. *J. Fluid Mech.* **542**, 365–379.

Billant, P. & Le Dizès, S. 2009 Waves on a columnar vortex in a strongly stratified fluid. *Phys. Fluids* **21**, 106602.

Boubnov, B. M., Gledzer, E. B. & Hopfinger, E. J. 1995 Stratified circular Couette flow: instability and flow regimes. *J. Fluid Mech.* **292**, 333–358.

Boulanger, N., Meunier, P. & Le Dizès, S. 2007 Structure of a tilted stratified vortex. *J. Fluid Mech.* **583**, 443–458.

Boulanger, N., Meunier, P. & Le Dizès, S. 2008 Instability of a tilted vortex in stratified fluid. *J. Fluid Mech.* **596**, 1–20.

Broadbent, E. G. & Moore, D. W. 1979 Acoustic destabilization of vortices. *Phil. Trans. R. Soc. Lond.* A **290**, 353–371.

Caton, F., Janiaud, B. & Hopfinger, E. J. 2000 Stability and bifurcations in stratified Taylor–Couette flows. *J. Fluid Mech.* **419**, 93–124.

Dubrulle, B., Marie, L., Normand, C., Richard, D., Hersant, F. & Zahn, J.-P. 2005 A hydrodynamic shear instability in stratified disks. *Astron. Astrophys.* **429**, 1–13.

Fabre, D., Sipp, D. & Jacquin, L. 2006 The Kelvin waves and the singular modes of the Lamb–Oseen vortex. *J. Fluid Mech.* **551**, 235–274.

Ford, R. 1994 The instability of an axisymmetric vortex with monotonic potential vorticity in rotating shallow water. *J. Fluid Mech.* **280**, 303–334.

Guimbard, D., Le Dizès, S., Le Bars, M., Le Gal, P. & Leblanc, S. 2010 Elliptic instability of stratified fluid in a rotating cylinder. *J. Fluid Mech.* **660**, 240–257.

Hayashi, Y.-Y. & Young, W. R. 1987 Stable and unstable shear modes of rotating parallel flows in shallow waters. *J. Fluid Mech.* **184**, 477–504.

Knessl, C. & Keller, J. B. 1995 Stability of linear shear flows in shallow water. *J. Fluid Mech.* **303**, 203–214.

Le Bars, M. & Le Gal, P. 2007 Experimental analysis of the stratorotational instability in a cylindrical Couette flow. *Phys. Rev. Lett.* **99**, 064502.

Le Dizès, S. & Billant, P. 2009 Radiative instability in stratified vortices. *Phys. Fluids* **21**, 096602.

Le Dizès, S. & Riedinger, X. 2010 The strato-rotational instability of Taylor–Couette and Keplerian flows. *J. Fluid Mech.* **660**, 147–161.

Lindzen, R. S. & Barker, J. W. 1985 Instability and wave over-reflection in stably stratified shear flow. *J. Fluid Mech.* **151**, 189–217.

Luo, K. H. & Sandham, N. D. 1997 Instability of vortical and acoustic modes in supersonic round jets. *Phys. Fluids* **9**, 1003–1013.

Meunier, P. & Leweke, T. 2003 Analysis and optimization of the error caused by high velocity gradients in particle image velocimetry. *Exp. Fluids* **35** (5), 408–421.

Molemaker, M. J., McWilliams, J. C. & Yavneh, I. 2001 Instability and equilibration of centrifugally stable stratified Taylor–Couette flow. *Phys. Rev. Lett.* **86**, 5270–5273.

Narayan, R., Goldreich, P. & Goodman, J. 1987 Physics of modes in a differentially rotating system: analysis of the shearing sheet. *Mon. Not. R. Astron. Soc.* **228**, 1–41.

Ooyama, K. 1966 On the stability of baroclinic circular vortex: a sufficient criterion for instability. *J. Atmos. Sci.* **23**, 43–53.

Parras, L. & Le Dizès, S. 2010 Temporal instability modes of supersonic round jets. *J. Fluid Mech.* **662**, 173–196.

Riedinger, X., Le Dizès, S. & Meunier, P. 2010*a* Viscous stability properties of a Lamb–Oseen vortex in a stratified fluid. *J. Fluid Mech.* **645**, 255–278.

Riedinger, X., Meunier, P. & Le Dizès, S. 2010*b* Instability of a vertical columnar vortex in a stratified fluid. *Exp. Fluids* **49**, 673–681.

Roberts, P. H. 2003 On vortex waves in compressible fluids. I. The hollow-core vortex. *Phil. Trans. R. Soc. Lond.* A **459**, 331–352.

Satomura, T. 1981 An investigation of shear instability in a shallow water. *J. Met. Soc. Japan* **59**, 148–167.

Schecter, D. A. 2008 The spontaneous imbalance of an atmospheric vortex at high Rossby number. *J. Atmos. Sci.* **65**, 2498–2521.

Schecter, D. A. & Montgomery, M. T. 2004 Damping and pumping of a vortex Rossby wave in a monotonic cyclone: critical layer stirring versus inertia–buoyancy wave emission. *Phys. Fluids* **16**, 1334–1348.

Shalybkov, D. & Rüdiger, G. 2005 Stability of density-stratified viscous Taylor–Couette flows. *Astron. Astrophys.* **438**, 411–417.

Thorpe, S. A. 1966 Notes on 1966 summer geophysical fluid dynamics, p. 80. Woods Hole Oceanographic Institute.

Withjack, E. M. & Chen, C. F. 1974 An experimental study of Couette instability of stratified fluids. *J. Fluid Mech.* **66**, 725–737.

Withjack, E. M. & Chen, C. F. 1975 Stability analysis of rotational Couette flow of stratified fluids. *J. Fluid Mech.* **68**, 157–175.

Yavneh, I., McWilliams, J. C. & Molemaker, M. J. 2001 Non-axisymmetric instability of centrifugally stable stratified Taylor–Couette flow. *J. Fluid Mech.* **448**, 1–21.